ISSN 1029-9599, Physical Mesomechanics, 2024, Vol. 27, No. 6, pp. 664–677. © Pleiades Publishing, Ltd., 2024.
Russian Text © The Author(s), 2024, published in Fizicheskaya Mezomekhanika, 2024, Vol. 27, No. 4, pp. 47–62.

Retained Austenite Transformation and Portevin–Le Chatelier Effect in 44CrMn2Si2Mo Steel under Tension

S. I. Borisov[1,2]*, Yu. I. Borisova[1,2], E. S. Tkachev[1,2], S. M. Gaidar[1], and R. O. Kaibyshev[1]

[1] *Russian State Agrarian University—Moscow Timiryazev Agricultural Academy, Moscow, 127434 Russia*
[2] *Belgorod National State Research University, Belgorod, 308015 Russia*
** e-mail: borisov_si@bsu.edu.ru*

Received February 1, 2024; revised April 12, 2024; accepted April 15, 2024

Abstract—The 44CrMn2Si2Mo steel heat treated by quenching and partitioning demonstrates a unique combination of strength characteristics: the yield stress $\sigma_{0.2} = 1140$ MPa, ultimate strength $\sigma_B = 1690$ MPa, and elongation $\delta = 20.7\%$. Quenching and partitioning leads to the formation of a multiphase structure consisting of primary martensite, retained austenite, bainite, and secondary martensite. Primary martensite and bainite contain transition-metal carbides Fe_2C. The high ductility of the steel is due to the transformation of retained austenite into strain-induced martensite during tension, which ensures high strain hardening. Stable plastic flow is observed at low strain, when a significant fraction of retained austenite is transformed into strain-induced martensite. The plastic flow instability, which appears as the Portevin–Le Chatelier effect on deformation curves and plastic flow localization in deformation bands, occurs at higher strains and is associated with the transformation of film-like retained austenite. The velocity of deformation bands decreases with a decrease in the volume fraction of retained austenite. Localization of plastic flow in the neck and fracture occur when the transformation of retained austenite into strain-induced martensite cannot provide strain hardening, and deformation bands lose their mobility.

Keywords: medium-carbon steel, quenching and partitioning, deformation localization, Portevin–Le Chatelier effect, TRIP effect

DOI: 10.1134/S1029959924060043

1. INTRODUCTION

As part of the development of third-generation advanced high-strength steels for the automotive industry, the quenching and partitioning (Q&P) heat treatment appeared for low-alloy steels [1–3]. These steels should combine high yield stress ($\sigma_{0.2} \geq 1000$ MPa) with high ductility. The product of (ultimate tensile) strength and elongation (ductility) (PSE) $\sigma_B\delta$ should be ≥ 30 GPa % for automotive steels [1]. No such combination of strength properties and ductility has been achieved in other types of automotive steels [1, 3]. Yield stresses of Q&P steels were relatively easily improved, but $\sigma_B\delta \geq 30$ GPa % could not be achieved for nearly 15 years [4–7]. The microstructural design of Q&P steels presents a multiphase structure consisting of low-carbon, low-temperature tempered primary martensite M1 with intermediate transition-metal carbides η-Fe_2C, bainitic ferrite, high-carbon retained austenite, and secondary martensite M2 [1–10]. In Q&P steels, primary martensite is believed to provide high strength properties, while high plasticity is due to retained austenite, which transforms into strain-induced martensite under tension. An increase in the steel plasticity due to the transformation of retained austenite into strain-induced martensite (transformation-induced plasticity (TRIP) effect) is associated with an increase in strain hardening, which prevents strain localization [1, 4, 7, 11]. In Q&P steels with 0.2 to 0.3% carbon, retained austenite is present in the form of films located along the boundaries of laths and blocks, and the $\sigma_B\delta$ value does not exceed 20 GPa % [9–12]. Film-like retained austenite is resistant to transformation into strain-induced martensite under tension [10, 11, 13]. In Q&P steels with ~0.4% carbon, retained austenite has the form of blocks, most of which is transformed into strain-induced martensite under tension, thus increasing the $\sigma_B\delta$ value above 30 GPa % [4, 5, 7].

Quenching and partitioning treatment consists in heating above the austenitization temperature follow-

ed by rapid cooling to the quenching temperature T_q. The quenching temperature should be below the martensite start temperature M_s and above the martensite finish temperature M_f (Fig. 1). During quenching, primary martensite is formed, and the quenching temperature largely determines the specific volume and morphology of retained austenite. Next, the steel is heated to the partitioning temperature T_p, which is usually higher than M_s, to redistribute carbon between martensite and retained austenite [1, 3–10]. Along with the saturation of the retained austenite with carbon, partitioning is accompanied by two processes: the precipitation of intermediate carbides in martensite and partial transformation of the retained austenite into bainite [6–8]. In Q&P steels with ≥1.5 wt % Si, bainite transformation occurs without the formation of cementite and consists in the formation of bainitic ferrite with transition-metal carbides η-Fe_2C located along the boundaries of bainitic ferrite plates [14, 15]. Saturation of the untransformed austenite with carbon reduces the martensite start temperature M_s, which increases its resistance to martensite transformation [15]. However, part of the retained austenite is transformed into secondary martensite upon cooling in air or quenching in water from the partitioning temperature [4, 7, 9, 15]. Secondary martensite is formed, as a rule, at temperatures below the temperature of precipitation of transition-metal carbides η-Fe_2C. This excludes self-tempering processes in it, and secondary martensite turns out to be supersaturated with carbon [15].

Plasticity of TRIP steels depends on many factors, such as the specific volume of retained austenite, its morphology, size, and carbon content [4, 7, 11, 16]. To study the transformation of retained austenite into strain-induced martensite under tension and its influence on plastic flow stability is an important task because this can not only give insight into the mechanisms of the $\sigma_B\delta$ improvement in low-alloy Q&P steels with ~0.4 wt % carbon but also optimize Q&P modes. In addition, special attention should be paid to the study of plastic flow localization and instability since these processes can cause the relief in the form of localized deformation bands on the steel surface, which excludes its use in cold drawing [1, 17]. The aim of this work is to study the structure evolution under tension and its effect on plastic flow localization in 44CrMn2Si2Mo steel subjected to Q&P. Particular attention is paid to the correlation of the transformation of retained austenite into strain-induced martensite with dynamic strain aging manifested as the Portevin–Le Chatelier effect [17, 18], as well as to the characteristics of deformation bands where plastic flow localizes.

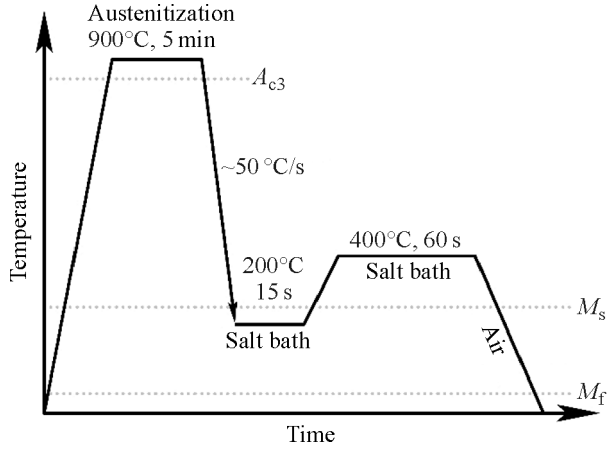

Fig. 1. Schematic of Q&P heat treatment.

2. MATERIAL AND METHODS OF INVESTIGATION

Experimental steel 44CrMn2Si2Mo with the chemical composition given in Table 1 was melted in an open induction furnace with subsequent electroslag remelting. The casting was homogenized at 1150°C for 4 h, followed by forging at 1150–950°C to the billet sizes $60 \times 150 \times 450$ mm^3 and air cooling. The billet was used to cut 3-mm-thick specimens, which were subjected to Q&P. This treatment consisted in austenitization at 900°C for 5 min with subsequent quenching in a salt bath heated to 200°C and holding in it for 15 s. This was followed by isothermal holding in the salt bath at 400°C for 60 s and air cooling (Fig. 1).

Samples for microstructural studies by scanning and transmission electron microscopy were prepared by electropolishing and double-jet electropolishing in an electrolyte consisting of 90% acetic and 10% perchloric acid, respectively. The prepared foils were examined under a JEOL JEM-2100 transmission electron microscope at an accelerating voltage of 200 kV. The microstructure was also studied under a FEI Quanta 600 FEG scanning electron microscope at a voltage of 20 kV equipped with an EDAX VelocityTM camera to plot electron backscatter diffrac-

Table 1. Chemical composition of the steel, wt %

Fe	C	Si	Mn	Cr	Mo
Base	0.44	1.8	1.3	0.82	0.28

tion (EBSD) maps. The tensor density of dislocations in martensite and austenite was calculated from EBSD orientation distribution maps [7, 15]:

$$\rho_{KAM} = \frac{2\theta_{KAM}}{bh}, \quad (1)$$

where θ_{KAM} is the average misorientation between adjacent points on the orientation distribution map at scan step h, and b is the Burgers vector.

Tensile tests were run on an Instron 5882 universal testing machine at room temperature with a constant strain rate of 1 mm/min. The gauge length of tensile specimens was 35 mm, and the cross section was 7×3 mm^2. Deformation band propagation in specimens tested to fracture was traced by the digital image correlation (DIC) method using the Vic-2D system, which allows for noncontact measurement of the strain distribution on the specimen surface and determines the local strain rate. For noncontact strain measurement along the gauge length, a speckle pattern was applied to the specimen surface, which is used as a grid for calculating local strain fields and strain rates. The surfaces of white-painted specimens were speckled by spraying black paint. Calculations were performed in Vic-2D software using 2448×2048 resolution images covering the entire gauge length of tensile specimens; the shooting speed was 2 frames per second. The initial size of subregions corresponding to the gauge length of specimens was $\sim 1200 \times 220$ pixels. Data processing and construction of strain localization maps were performed using the MATLAB software package. Deformation bands were registered from the beginning of tension to fracture of specimens. To study microstructural evolution, tension of two specimens was stopped at the strain rates 0.6 and 7.0%. The uniform elongation of a test specimen was 17.0%. Microstructural studies by transmission electron microscopy and EBSD after deformation were performed on samples cut from the uniformly elongated region.

The volume fraction of retained austenite was determined from X-ray diffraction (XRD) analysis using a Rigaku Ultima IV diffractometer with $CuK_{\alpha 1}$ radiation in the range $2\theta = 35°–105°$ at the scan rate 1°/min by comparing the integral intensities of the $(200)_{\alpha'}$, $(211)_{\alpha'}$ and $(220)_{\alpha'}$ peaks from martensite with the $(200)_\gamma$, $(220)_\gamma$ and $(311)_\gamma$ peaks from austenite [7, 19]:

$$V_\gamma = \frac{\sum_{i=1}^{3}(I_i^{(\gamma)}/R_i^{(\gamma)})}{\sum_{i=1}^{3}(I_i^{(\alpha')}/R_i^{(\alpha')}) + \sum_{i=1}^{3}(I_i^{(\gamma)}/R_i^{(\gamma)})}, \quad (2)$$

where I is the integral peak intensity, and R is the theoretical peak intensity.

The average concentration of carbon in retained austenite C_γ was determined by the following formula [7, 19]:

$$a_\gamma(\text{Å}) = 3.578 + 0.033C_\gamma + 0.00095Mn_\gamma + 0.0031Mo_\gamma, \quad (3)$$

where a_γ is the lattice parameter of austenite, Mn_γ and Mo_γ are the concentrations of the respective elements in the retained austenite, which is taken as their concentrations in the steel because no redistribution of substitutional elements occurs at the partitioning temperature.

Dilatometric studies were carried out on cylindrical specimens 10 mm long and 3 mm in diameter using a Bahr DIL 805 quenching dilatometer (TA Instruments). The tests were carried out in a mode simulating Q&P treatment: heating to 900°C at the rate 10 °C/s and holding at this temperature for 5 min (stage 1); cooling to 200°C at the rate 50 °C/s and holding for 15 s (stage 2); heating to 400°C, holding for 60 s, and cooling to room temperature at the rate 5 °C/s (stage 3) (Fig. 2). Volume fractions of the microstructural constituents, excluding retained austenite, were determined from dilatometric analysis by the lever rule based on two straight lines representing the thermal expansion of austenite (the portion of cooling from 900°C to the quenching temperature) and ferrite martensite (the portion of cooling from the partitioning temperature 400°C to room temperature). The curve obtained by this method was reconstructed in terms of retained austenite determined in the steel by XRD analysis (Fig. 2b).

3. RESULTS AND DISCUSSION

3.1. Phase Composition and Microstructure of Q&P steel

The critical points $A_{c1} = 760$°C and $A_{c3} = 857$°C were determined from calorimetric studies, and the martensite start and finish temperatures $M_s = 270$°C and $M_f = 51$°C were taken from [7]. Thus, holding at 900°C produces a fully austenitic structure before quenching. Dilatometric analysis showed that, during quenching, the martensite transformation occurs in the temperature range 270–200°C (Fig. 2). During isothermal holding at 200°C, the specimen noticeably grows in length, which can be associated with the enrichment of the retained austenite with carbon, bainite transformation, or isothermal martensite transformation (Fig. 2b) [20–22]. In the previous work [23], it was shown that carbon redistribution during tempering at 200°C after water quenching is a very slow process. Consequently, the saturation of the re-

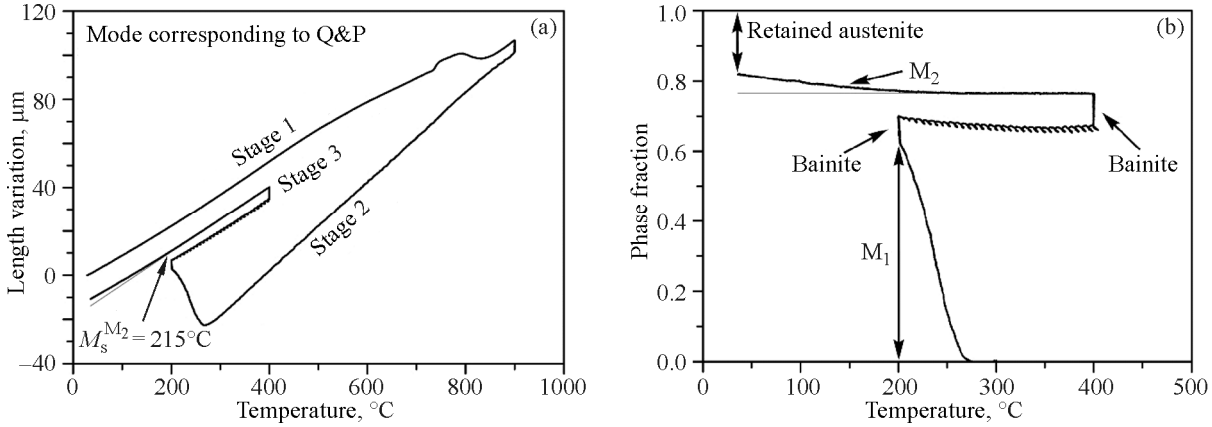

Fig. 2. Dilatometric curve obtained in the mode simulating Q&P: stage 1—austenitization (heating to 900°C, holding for 5 min), stage 2—quenching at $T_q = 200$°C (cooling at the rate 50 °C/s), stage 3—partitioning at $T_p = 400$°C (a); phase fractions obtained from dilatometric analysis using the lever rule (b).

tained austenite with carbon cannot lead to the specimen elongation during isothermal holding at 200°C for 15 s. However, isothermal martensite transformations or bainite transformations are possible. In low-alloy steels, martensite transformations are usually athermal [24]. Isothermal martensite transformations were found only in hypereutectoid steels and steels with a high content of Mn, Ni and Cr [24, 25]. Thus, elongation of the studied steel specimens during short isothermal holding at 200°C can be associated with the formation of bainitic ferrite. When heated to the partitioning temperature, the specimen shortens (Fig. 2b), which is usually associated with the precipitation of intermediate carbides, which decreases the carbon content in the martensitic matrix. At stage 3, during partitioning, the specimen elongation can be associated both with the saturation of the retained austenite with carbon and with the bainite transformation [20–22]. In this case, the increase in volume due to carbon redistribution from martensite to austenite is significantly less than that due to the formation of bainitic ferrite. This allows the fraction of bainite to be determined from the dilatometric curve if the bainite transformation occurs at the partitioning temperature [26]. During air cooling from the partitioning temperature to room temperature, the specimen length also increases noticeably below the temperature 215°C. This is the secondary martensite start temperature. The shape of the curve during cooling from the partitioning temperature clearly indicates a partial transformation of the retained austenite into secondary martensite. Thus, Q&P results in a multiphase structure consisting of primary martensite, bainitic ferrite, secondary martensite, and retained austenite. According to dilatometry, the fraction of primary martensite is 0.63 alone and 0.70 together with bainite formed during isothermal holding at stage 2. The total fraction of bainite in the treated structure is 0.14. The fraction of secondary martensite is 0.05, and that of retained austenite is 0.18.

The volume fraction of primary martensite (f^{M_1}) and untransformed austenite ($1 - f^{M_1}$) after quenching can be theoretically calculated using the Koistinen–Marburger (K–M) relation [9, 10, 27]:

$$f^{M_1} = 1 - \exp(-1.1 \times 10^{-2}(M_s - T_q)). \quad (4)$$

The value predicted by Eq. (4) is $f^{M_1} = 0.54$, which is 0.09 lower than the value experimentally measured for martensite formed during cooling at stage 2 (Fig. 2). Consequently, the fraction of retained austenite after quenching to 200°C is estimated as $f^{\gamma} = 0.46$. This equation is inapplicable to estimating the increase in the specific volume of martensite during isothermal holding [27].

The possibility of martensite transformation can be estimated by the empirical relationship proposed in [28]:

$$M_s = 539 - 423C_C - 30.4C_{Mn} - 12.1C_{Cr} - 7.5C_{Mo}, \quad (5)$$

where M_s is the martensite start temperature, °C; C_C, C_{Mn}, C_{Cr}, and C_{Mo} are the concentrations of the respective elements, wt %. The value $M_s = 282$°C was obtained by Eq. (5), which is only 12°C higher than the experimental value. This equation can be used to estimate the carbon concentration in secondary martensite by $M_s = 215$°C. The calculated carbon concentration in martensite is 0.63%, i.e. it is significantly lower than the carbon concentration in retained austenite at room temperature (Table 2). For retained austenite with 1.4% carbon, $M_s = -105$°C, which is

Table 2. Microstructural parameters of the steel at different strains

Strain, %	Volume fraction of retained austenite (EBSD)	Volume fraction of retained austenite (XRD)	Average size of austenite islands (EBSD), μm	Dislocation density in martensite (EBSD), 10^{14} m^{-2}	Dislocation density in austenite (EBSD), 10^{14} m^{-2}	Carbon concentration in retained austenite (XRD), wt %
0.0	0.236	0.18	2.7	5.8	6.5	1.4
0.6	0.063	0.15	1.4	6.3	6.5	1.5
7.0	0.021	0.09	1.2	6.6	6.4	1.7
17.0	0.016	<0.03	0.9	7.6	6.8	–

below room temperature. For $M_s = 20$°C, the carbon content is 1.1%. Therefore, secondary martensite can only be formed from retained austenite in which the carbon content varies from 0.63 to 1.1 wt %. The formation of secondary martensite indicates a nonuniform distribution of carbon in the retained austenite after partitioning.

The possibility of bainite transformation was assessed by calculating the bainite start temperature B_s using the formula proposed in [29], which accurately predicts the B_s value in steels with less than 1 wt % carbon and more than 0.5 wt % Si:

$$B_s = 839 - 86C_{Mn} - 67C_{Cr} - 75C_{Mo} + 23C_{Si} - 271(1 - \exp(-1.33C_C)), \quad (6)$$

where C_{Si} is the silicon concentration, wt %.

The bainite start temperature was calculated to be $B_s = 570$, 463, and 388°C for the carbon concentrations 0.44, 1.4, and 1.6% (Table 2), respectively. Therefore, bainite transformation at 400°C is possible only in retained austenite with less than 1.5 wt % carbon.

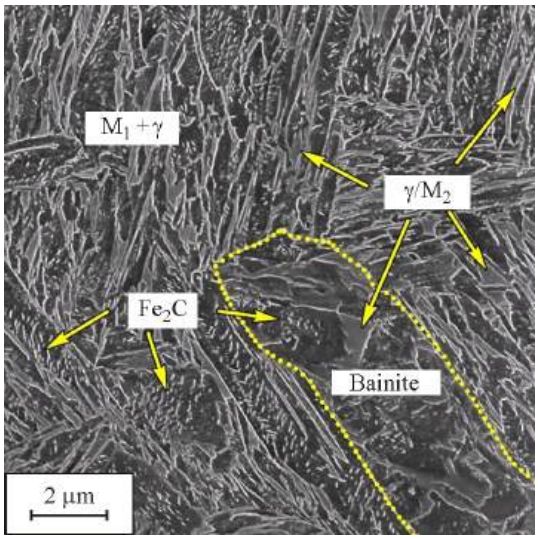

Fig. 3. Microstructure of the Q&P steel. Scanning electron microscopy (color online).

Figure 3 shows the microstructure of the steel after Q&P. Dark regions of primary martensite and bainitic ferrite are strongly etched because they are depleted of carbon. Bright regions of secondary martensite and retained austenite enriched in carbon have a high resistance to chemical etching [15, 30]. The regions of secondary martensite and retained austenite (γ/M_2), which are poorly distinguishable by scanning electron microscopy, are located in the matrix of primary martensite and have an irregular shape. Primary martensite has a three-level hierarchy typical of packet martensite: original austenite grains, packets, and blocks [12]. The martensite blocks contain elongated carbides. The γ/M_2 regions are located either along the boundaries of packets or inside them as irregular blocks.

The phase map (Fig. 4a) confirms that the retained austenite is located both inside primary martensite in block chains and along its packet boundaries. EBSD analysis gave overestimated values of the specific volume of retained austenite (Table 2). At the same time, it is known [31] that the XRD-determined values of the specific volume of retained austenite are always higher than those found by the EBSD method because the latter sums the retained austenite of both block and film morphology, while EBSD maps represent only block austenite. The thickness of austenite films is under 200 nm (Fig. 5b), which is less than the resolving power of the EBSD method. At the same time, the bainitic ferrite plates are also thinner than 300 nm (Fig. 5a) and cannot be detected by EBSD. Consequently, the retained austenite regions visible on the EBSD maps include bainitic ferrite plates, which gives the overestimated specific volume of retained austenite compared to the X-ray diffraction data (Table 2).

The dislocation density in martensite and block retained austenite is the same (Table 2). Along with

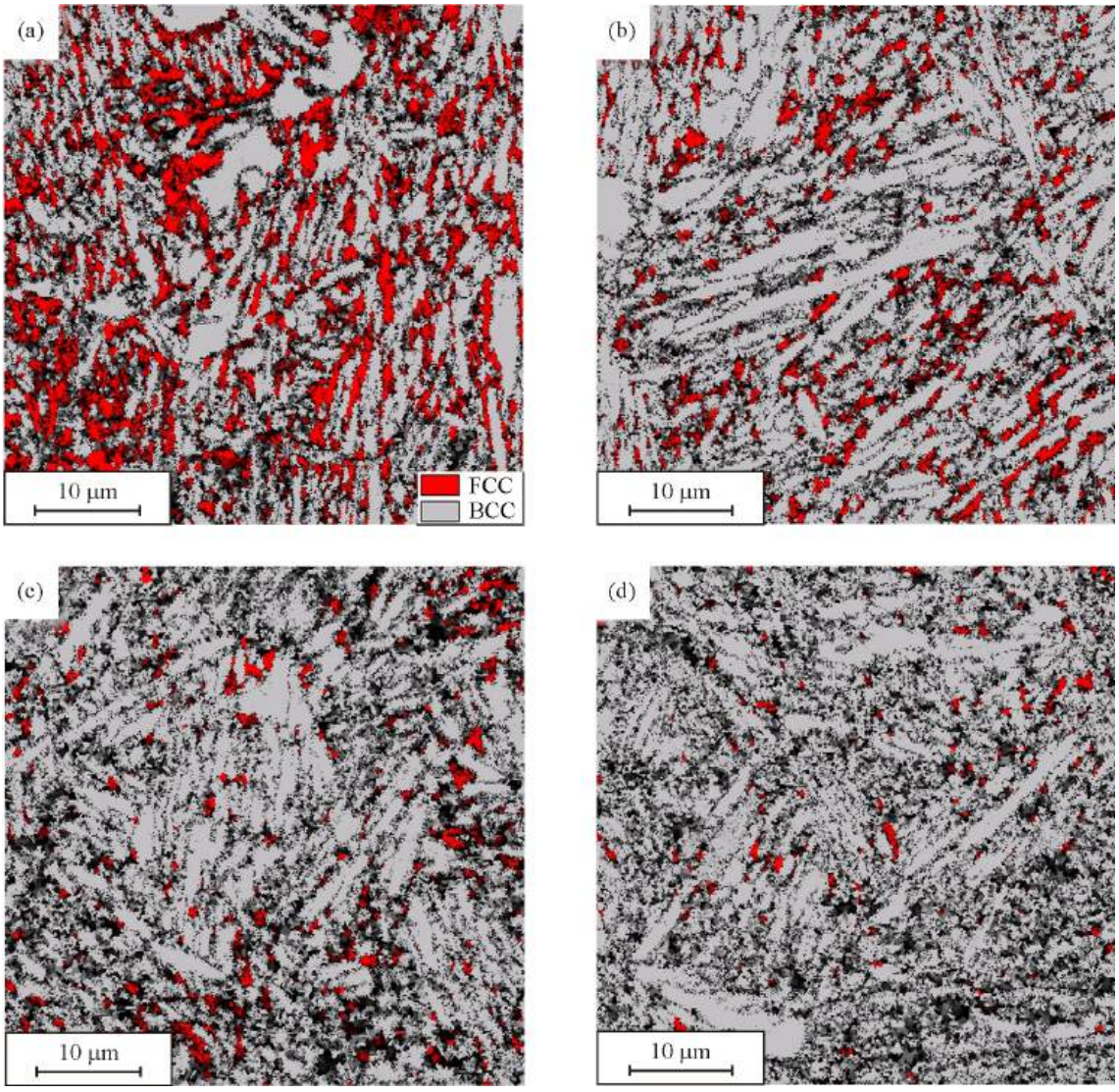

Fig. 4. EBSD phase maps of the steel in the initial state (a) and strained to 0.6 (b), 7.0 (c), and 17.0% (d) (color online).

the dislocation substructure, martensite laths contain twins about 20 nm in thickness and up to several microns in length. Despite the high dislocation density, the diffraction contrast is uniform (Fig. 5a). This indicates that the lattice characterized by ρ_{KAM} is distorted in small structural elements, such as martensite blocks. The high dislocation density found in the retained austenite contradicts the assumptions about the low dislocation density in retained austenite in Q&P steels [9].

3.2. Mechanical Properties

The Q&P steel has the yield stress $\sigma_{0.2}$ = 1140 MPa, tensile strength σ_B = 1690 MPa, and relative elongation to fracture of 20.7%. The product of ultimate strength and ductility $\sigma_B\delta$ for the studied steel is 35 GPa %. Thus, the steel meets all the requirements for third-generation advanced high-strength steels [1]. The deformation curve is shown in Fig. 6. It is evident that there is no static strain aging, and the steel exhibits continuous plastic flow near the yield stress [17, 18]. According to the deformation curve, plastic flow is unstable during tension (Portevin–Le Chatelier effect) and is characterized by flow stress jumps above the σ–ε curve level and subsequent drops below the general stress level (Fig. 6a). This jerky deformation referred to as the Portevin–Le Chatelier effect is characteristic of type A plastic flow instability. Type A is associated with quasi-continuous propagation of localized plastic deformation bands in a specimen under tension [18, 32]. The σ–ε

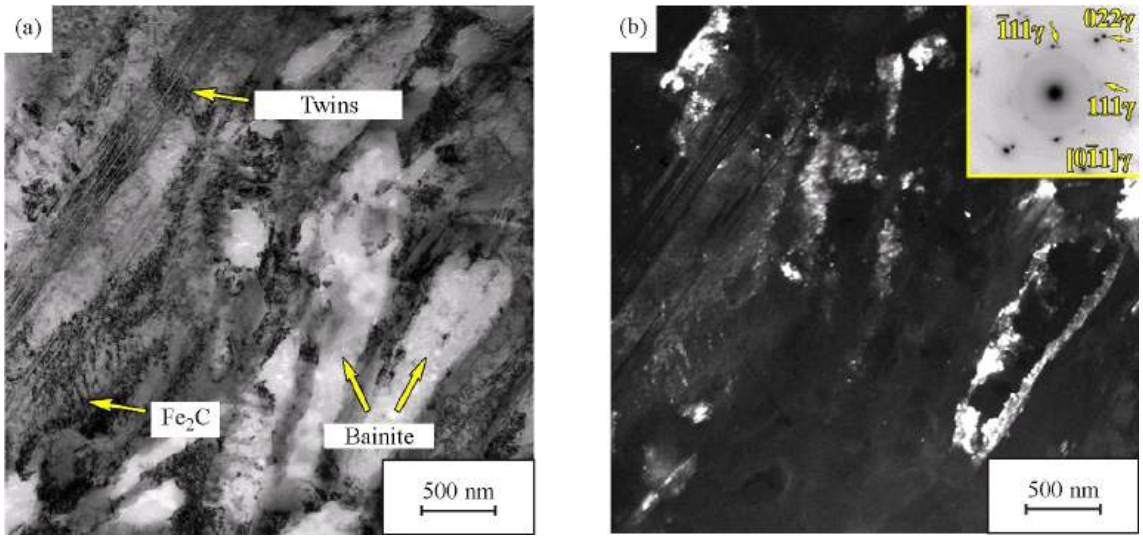

Fig. 5. Microstructure of the Q&P steel (a), dark-field image of retained austenite (b). Transmission electron microscopy (color online).

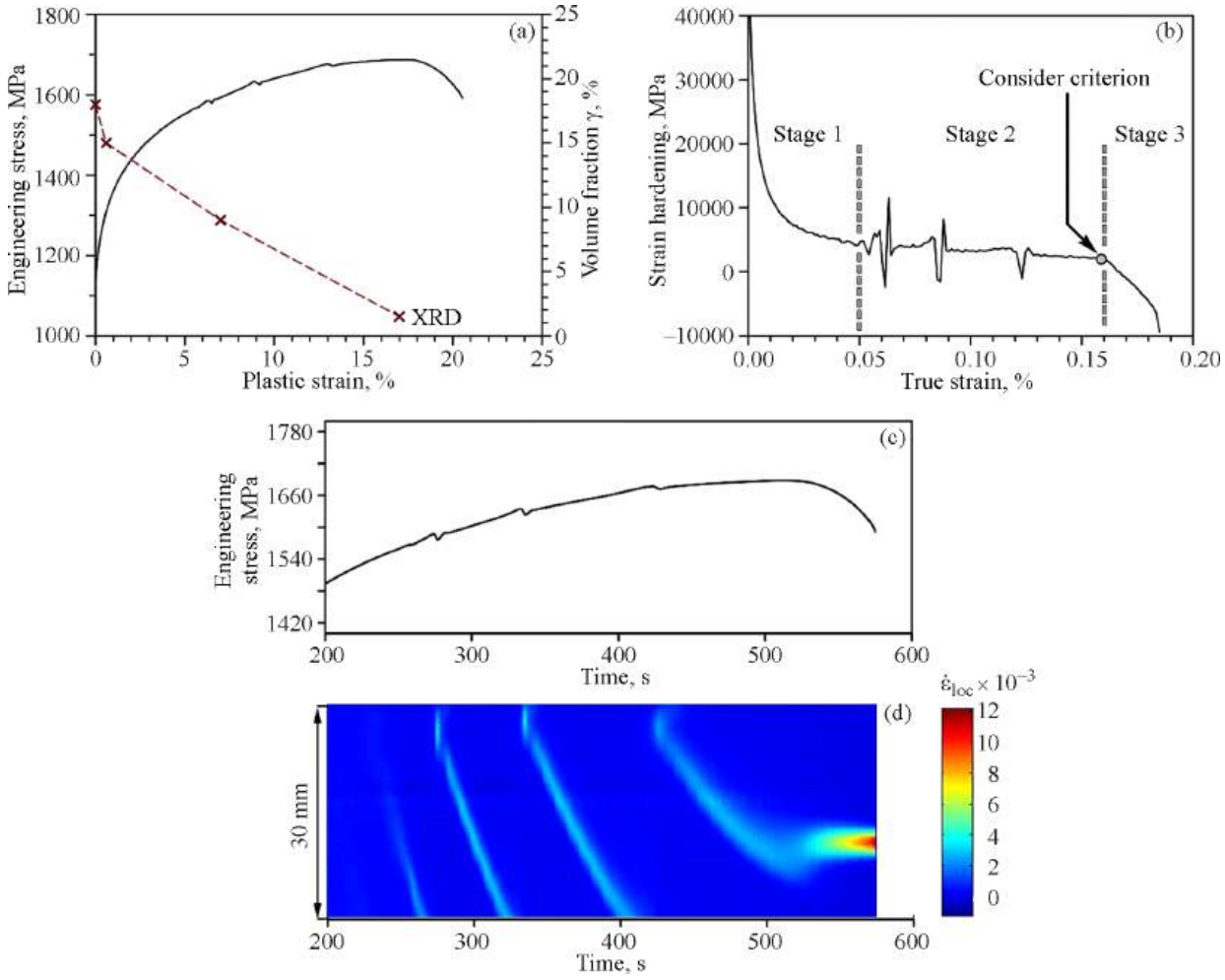

Fig. 6. Stress–plastic strain curves and strain dependence of the volume fraction of retained austenite (a); strain hardening–true strain curve (b); dependence of stress on the test time (c); the corresponding map of time variation in the local strain rate along the tensile axis (d) (color online).

curve behavior is typical of this type of plastic flow instability up to the strain 15.0%. The portion characterized by high strain hardening and a smooth σ–ε curve precedes the portion of jerky flow. Unstable plastic flow manifests itself only upon reaching a certain critical strain equal to 6.3%, with the amplitude of flow stress jumps being about 10 MPa. However, a small number of jumps on the σ–ε curve and their absence at strains above 15.0% are not typical of this type of plastic flow instability. Type A is characterized by an increase in the number of jumps with strain. For type A, stress oscillations are observed until the specimen fails [18, 32].

The dependence of strain hardening on strain has three stages (Fig. 6b). At the first stage, the strain hardening value dσ/dε decreases until the strain 5.0%, which is slightly below the critical value, i.e. the first stage almost coincides with the stage at which stress jumps are not observed. The second stage is characterized by $d\sigma/d\varepsilon \sim 4000$ MPa, which weakly depends on the strain up to 17.0%. This value is slightly higher than the strain at which stress jumps disappear. Stress oscillations occur at the second stage. The third stage is characterized by a drop in dσ/dε. This stage correlates with a decrease in the flow stress upon achieving the ultimate strength. An intense drop in both strain hardening and flow stress begins on meeting the Consider criterion (Figs. 6a–6c) [17]:

$$\frac{d\sigma}{d\varepsilon} = \sigma, \tag{7}$$

i.e. necking begins in the specimen when strain hardening cannot make the neck stronger than the uniformly elongated region. This causes localization of plastic deformation.

Localization of plastic flow in deformation bands was estimated using local strain rate maps showing the variation in the local strain rate distribution along the tensile axis during testing. Figures 6c and 6d show the deformation curve portion and the corresponding local strain rate map. The time interval of deformation bands on the local strain rate map was chosen so that deformation bands were clearly visible. The results obtained indicate that each stress drop on the deformation curve corresponds to the formation of a new deformation band, which is followed by its propagation accompanied by strain hardening, i.e. the appearance of stress jumps on the σ–ε curve is associated with plastic flow localization in the deformation band. Consequently, stage 1 is the stage of uniform deformation of the specimen, and stage 2 is the stage of propagation of localized plastic deformation bands. An increase in flow stresses is required for localization to begin, and band propagation occurs at lower flow stresses. The velocity of band propagation decreases with strain. For the first and subsequent bands, the band velocity is 0.80, 0.55, 0.41, and 0.26 mm/s, respectively. It is evident from Fig. 6d that the first band originates in the middle of the specimen and moves toward its lower part. Subsequent deformation bands are initiated on the opposite part of the specimen. After a short propagation of the last band, it stops closer to the specimen center, followed by necking and fracture. The band arrest correlates with the disappearance of stress jumps and the fulfillment of the Consider criterion, i.e. a localized deformation band stops because strain hardening in it induced by plastic flow localization cannot provide strength above the Consider criterion.

3.3. Microstructure after Tension

Tension causes a decrease in the specific volume of retained austenite, which is noticeable already at low strain (0.6%) (Table 2). Moreover, the specific volume of block retained austenite determined by the EBSD method decreases by 4 times (Fig. 4b), while the fraction of retained austenite determined by XRD analysis decreases by only 0.03. This means that EBSD analysis gives an underestimated value compared to the XRD method, as in most works on Q&P steels [31]. Microstructural studies by transmission electron microscopy reveal no significant macroheterogeneities in the uniformly elongated region of tensile specimens. Transmission electron microscopy shows that the regions of retained austenite are separated by the blocks of strain-induced martensite (Fig. 7). As a result, the elongated/continuous chains of retained austenite blocks on the EBSD map are divided into individual near-rectangular blocks (Fig. 4b), i.e. a significant drop in the volume of retained austenite according to the EBSD data is apparent. The size of integral blocks of retained austenite is reduced, which does not allow the EBSD analysis software to interpret them as austenite on account of the limited size resolution, in view of strong lattice bending of the retained austenite. The separation of retained austenite blocks by the structural elements of strain-induced martensite leads to an almost twofold decrease in their size, which increases the strength of retained austenite [7]. The structure contains primary martensite with transition-metal carbides η-Fe_2C, which have a lamellar shape, and secondary martensite/strain-induced martensite, with no carbides in the matrix (Figs. 7a–7d). Along with the replacement of

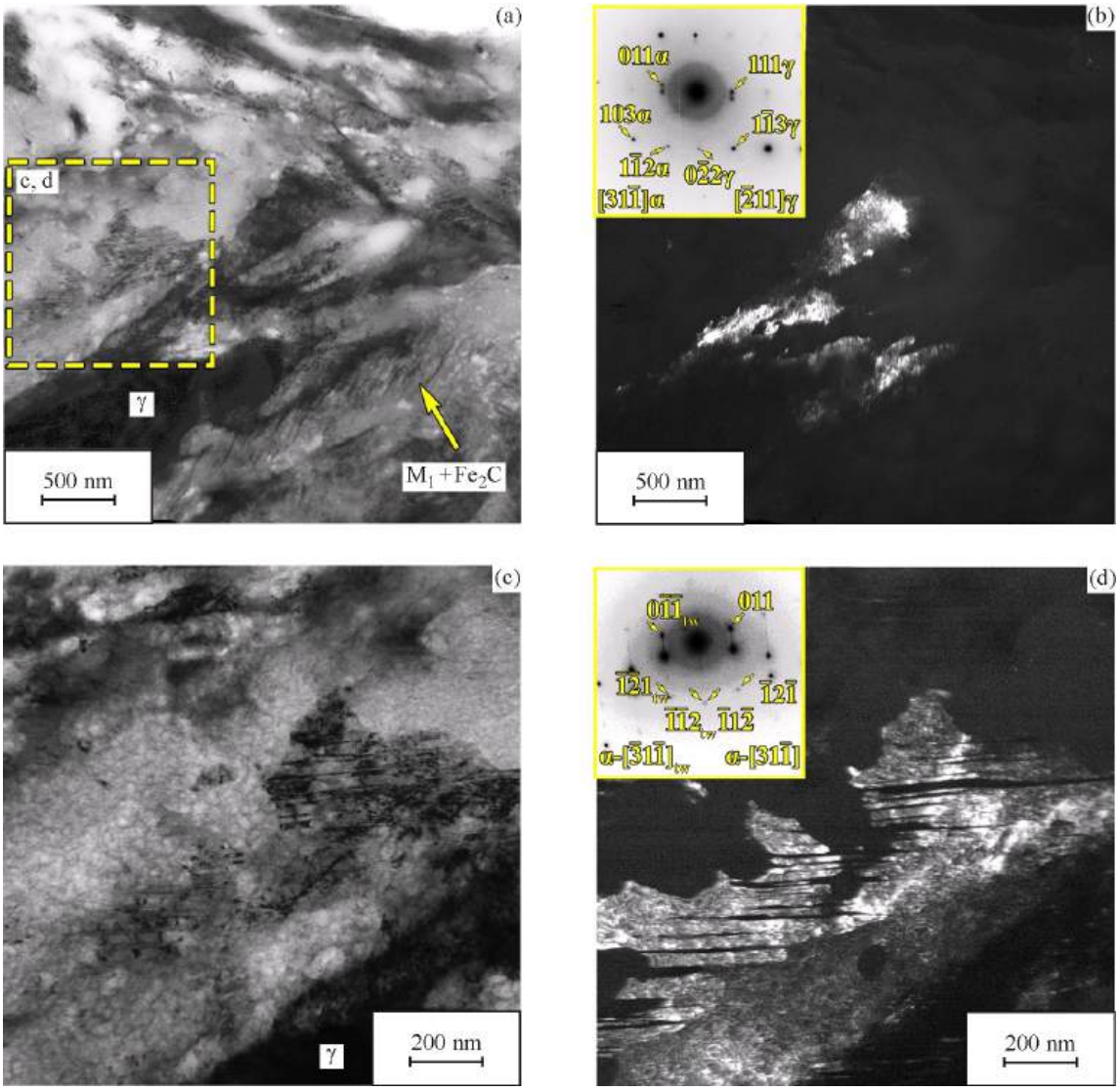

Fig. 7. Microstructure of the steel strained to 0.6% (a), dark-field image of retained austenite (b), strain-induced martensite (c, d) (color online).

weaker austenite by stronger martensite, this leads to a significant increase in strength. Moreover, the density of twins in strain-induced martensite or secondary martensite is high (Figs. 7c, 7d), which additionally strengthens martensite. Thus, high strain hardening at the initial stages of deformation is due to a simultaneous increase in the strength of martensite and retained austenite, and not only to the formation of strain-induced martensite.

The transformation of retained austenite into strain-induced martensite is the main process of structural evolution at the first stage, which ends when the specific volume of block retained austenite becomes less than that of film-like retained austenite (Fig. 8). The specific volumes of retained austenite determined by EBSD and XRD differ by four times above the strain 7.0% (Table 2). The EBSD method reveals individual blocks of retained austenite located mainly along the packet boundaries (Fig. 4c). An increase in the average carbon concentration in the retained austenite during deformation indicates that blocks of low-carbon retained austenite are first transformed into strain-induced martensite. In this case, the carbon concentration in the film-like retained austenite is higher than that in the retained austenite. This factor, along with the high dislocation density and more than 100 nm thickness, determines the stability of film-like austenite to transformation into strain-induced martensite [13]. After the first stage, most of the retained austenite is in the form of films (Fig. 8b).

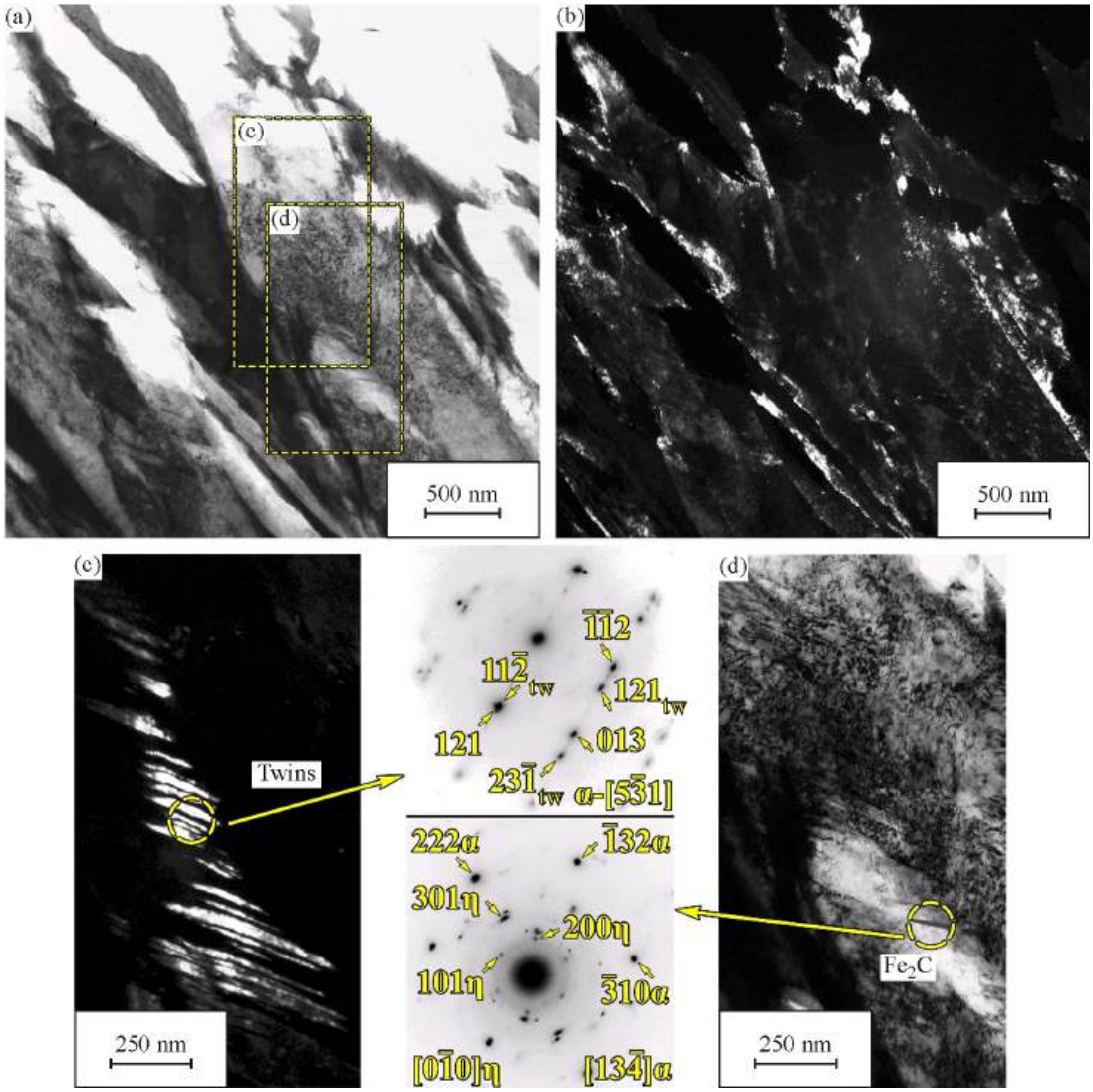

Fig. 8. Microstructure of the steel strained to 7.0% (a); dark-field image of film-like retained austenite (b); short twins in martensite (c); carbides in primary martensite (d) (color online).

The formation of twins less than 20 nm in thickness (Fig. 8c) and an increase in the dislocation density in martensite require an increase in stresses, as well as the formation of strain-induced martensite in retained austenite with more than 1.7 wt % carbon. The transition to the second stage occurs when plastic flow localization, which increases stresses, becomes a necessary condition for these processes to occur.

At the second stage of tension, the specific volume of retained austenite decreases by more than 3 times. Since the specific volume of block retained austenite revealed by the EBSD method decreased by only a quarter (Fig. 4d, Table 2), then strain-induced martensite was formed at this stage from film-like or block retained austenite, which was divided into regions less than 200 nm in size (Fig. 9b) by strain-induced martensite. It can be assumed that the preservation of individual blocks of untransformed austenite after the strain 17.0% (Figs. 4d, 9a–9d) is associated with the carbon concentration above 1.7 wt % and size less than 1 μm, which ensures high stability of this structural component [7]. In [33], it was shown that, at the carbon concentration above 1.8%, strain-induced martensite did not form during cold plastic deformation. At the second stage, both the retained austenite, which can be transformed into strain-induced martensite under high stresses, and the possibility of a further increase in the dislocation density in martensite are exhausted. Since only high-carbon retained austenite remains above the strain 17.0%, twinning develops in it (Fig. 9e), instead of forming strain-induced martensite. Twinning also en-

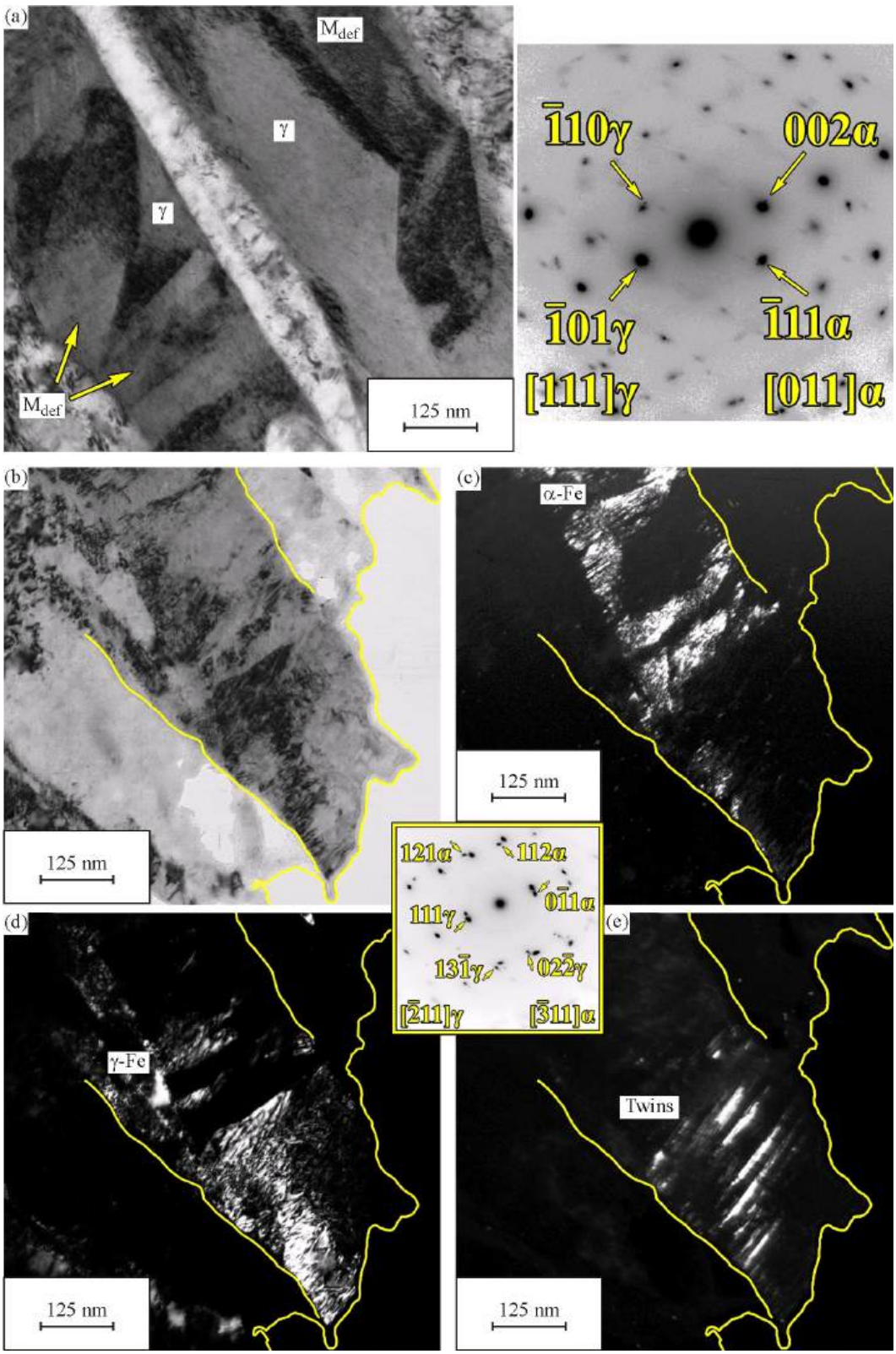

Fig. 9. Microstructure of the steel strained to 17.0% (a, b); dark-field images of strain-induced martensite (c), retained austenite (d), twins in retained austenite (e) (color online).

sures high strengthening of austenite [34]. However, the insignificant specific volume of the retained untransformed austenite with high carbon concentration cannot provide strain hardening by this mechanism. The third stage occurs when the localized deformation band loses mobility, which leads to necking and fracture.

4. CONCLUSIONS

Low-alloy steel 44CrMn2Si2Mo demonstrated a unique combination of high yield stress (1140 MPa), ultimate strength (1690 MPa), and ductility (δ = 20.7%, $\sigma_B\delta$ = 35 GPa %), which was explained by high strain hardening.

Along with the formation of martensite during cooling from the martensite start temperature 270°C to the quenching temperature 200°C, a phase transformation occurred during isothermal holding at the quenching temperature. After quenching, the volume fraction of untransformed austenite was approximately 0.30. Partitioning at 400°C for 60 s was accompanied by three simultaneous processes: carbon redistribution from martensite to retained austenite, precipitation of transition-metal lamellar carbides η-Fe_2C in martensite, and bainite transformation, resulting in bainitic ferrite. During air cooling after partitioning, secondary martensite was formed.

The steel structure after Q&P consisted of primary martensite, bainite, retained austenite, and a small amount of secondary martensite. The distribution of carbon in the volume of austenite after partitioning was nonuniform, which lead to the formation of secondary martensite with 0.63 wt % carbon. Austenite in the form of films was located along the boundaries of the martensite structure, while large islands of retained austenite of block morphology with the average size 2.7 μm were located between the blocks of primary martensite. The dislocation density in martensite and block retained austenite was the same. The carbon concentration in film-like retained austenite was higher than in block retained austenite. Under tension, strain-induced martensite was first formed in low-carbon retained austenite, and, with increasing flow stresses, in high-carbon retained austenite. When the carbon concentration in retained austenite exceeded 1.7 wt %, the formation of strain-induced martensite was replaced by twinning.

Three stages were distinguished on the tensile curves. The first stage was characterized by a very high value of strain hardening, which decreased with strain. A high value of strain hardening ensured uniform plastic flow. The main process at this stage was the separation of large islands of block retained austenite by strain-induced martensite into smaller islands with subsequent transformation of these islands into strain-induced martensite. The second stage was characterized by a slight decrease in the value of strain hardening. At this stage, plastic flow localized in deformation bands. The main process of microstructural evolution was the transformation of retained austenite into strain-induced martensite. Twinning and an increase in the dislocation density occurred in martensite. The third stage was accompanied by the loss of mobility of the localized plastic deformation band, which lead to necking and fracture. Before the third stage, the amount of retained austenite was insignificant, twinning and the formation of strain-induced martensite could not provide the required value of strain hardening. Loss of plastic flow stability occurred on meeting the Consider criterion.

At the second stage, stress jumps on the tensile curve correlated with strain localization in a deformation band since the formation of strain-induced martensite in retained austenite thinner than 200 nm required an increase in flow stresses. Type A plastic flow instability occurred on the σ–ε curves. The velocity of the deformation band decreased with strain. The formation of strain-induced martensite lead to a decrease in the volume fraction of retained austenite from 0.18 in the initial state to 0.03 at the strain 17.0%.

FUNDING

The work was financially supported by the Ministry of Science and Higher Education of the Russian Federation, grant No. 075-15-2021-572 dated 31.05.2021.

CONFLICT OF INTEREST

The authors of this work declare that they have no conflicts of interest.

REFERENCES

1. Fonstein, N., *Advanced High Strength Sheet Steels*, New York: Springer, 2015. https://doi.org/10.1007/978-3-319-19165-2
2. Matlock, D.K. and Speer, J.G., Third Generation of AHSS: Microstructure Design Concepts, in *Microstructure and Texture in Steels and Other Materials*, London: Springer, 2009, pp. 185–205. https://doi.org/10.1007/978-1-84882-454-6_11

3. Zhao, J. and Jiang, Z., Thermomechanical Processing of Advanced High Strength Steels, *Prog. Mater. Sci*., 2018, vol. 94, pp. 174–242. https://doi.org/10.1016/j.pmatsci.2018.01.006
4. Dai, Z., Chen, H., Ding, R., Lu, Q., Zhang, C., Yang, Z., and van der Zwaag, S., Fundamentals and Application of Solid-State Phase Transformations for Advanced High Strength Steels Containing Metastable Retained Austenite, *Mater. Sci. Eng. R. Rep*., 2021, vol. 143, p. 100590. https://doi.org/10.1016/j.mser.2020.100590
5. Li, H.Y., Lu, X.W., Li, W.J., and Jin, X.J., Microstructure and Mechanical Properties of an Ultrahigh-Strength 40SiMnNiCr Steel during the One-Step Quenching and Partitioning Process, *Metall. Mater. Trans. A*, 2010, vol. 41, pp. 1284–1300. https://doi.org/10.1007/s11661-010-0184-8
6. Santofimia, M.J., Zhao, L., and Sietsma, J., Overview of Mechanisms Involved during the Quenching and Partitioning Process in Steels, *Metall. Mater. Trans. A*, 2011, vol. 42, pp. 3620–3626. https://doi.org/10.1007/s11661-011-0706-z
7. Mishnev, R., Borisova, Y., Gaidar, S., Kniaziuk, T., Vagina, O., and Kaibyshev, R., Q&P Response of a Medium Carbon Low Alloy Steel, *Metals*, 2023, vol. 13, no. 4, p. 689. https://doi.org/10.3390/met13040689
8. Speer, J.G., De Moor, E., Findley, K.O., Matlock, D.K., De Cooman, B.C., and Edmonds, D.V., Analysis of Microstructure Evolution in Quenching and Partitioning Automotive Sheet Steel, *Metall. Mater. Trans. A*, 2011, vol. 42, pp. 3591–3601. https://doi.org/10.1007/s11661-011-0869-7
9. Seo, E.J., Cho, L., Estrin, Y., and De Cooman, B.C., Microstructure-Mechanical Properties Relationships for Quenching and Partitioning (Q&P) Processed Steel, *Acta Mater.*, 2016, vol. 113, pp. 124–139. https://doi.org/10.1016/j.actamat.2016.04.048
10. Tkachev, E., Borisov, S., Borisova, Y., Kniaziuk, T., Gaidar, S., and Kaibyshev, R., Strength–Toughness of a Low-Alloy 0.25C Steel Treated by Q&P Processing, *Materials*, 2023, vol. 16, no. 10, p. 3851. https://doi.org/10.3390/ma16103851
11. Soleimani, M., Kalhor, A., and Mirzadeh, H., Transformation-Induced Plasticity (TRIP) in Advanced Steels: A Review, *Mater. Sci. Eng. A*, 2020, vol. 795, p. 140023. https://doi.org/10.1016/j.msea.2020.140023
12. Kitahara, H., Ueji, R., Tsuji, N., and Minamino, Y., Crystallographic Features of Lath Martensite in Low-Carbon Steel, *Acta Mater.*, 2006, vol. 54, no. 5, p. 12791288. https://doi.org/10.1016/j.actamat.2005.11.001
13. Nakada, N., Ishibashi, Y., Tsuchiyama, T., and Takaki, S., Self-Stabilization of Untransformed Austenite by Hydrostatic Pressure via Martensitic Transformation, *Acta Mater.*, 2016, vol. 110, pp. 95–102. https://doi.org/10.1016/j.actamat.2016.03.048
14. Bhadeshia, H., Physical Metallurgy of Steels, in *Physical Metallurgy*, Elsevier, 2014, pp. 2157–2214. https://doi.org/10.1016/B978-0-444-53770-6.00021-6
15. Tkachev, E., Borisov, S., Borisova, Y., Kniaziuk, T., and Kaibyshev, R., Relationships between Strength, Ductility and Fracture Toughness in a 0.33C Steel after Quenching and Partitioning (Q&P) Treatment, *Crystals*, 2023, vol. 13, no. 10, p. 1431. https://doi.org/10.3390/cryst13101431
16. Chen, K., Jiang, Z., Liu, F., Li, H., Kang, C., Zhang, W., and Wang, A., Achievement of High Ductility and Ultra-High Strength of V-Nb Microalloyed Spring Steel by Austempered Multiphase Microstructure, *Metall. Mater. Trans. A*, 2020, vol. 51, pp. 3565–3575. https://doi.org/10.1007/s11661-020-05777-2
17. Krauss, G., *Steels: Processing Structure and Performance*, Materials Park, OH, USA: ASM Int., 2005. https://doi.org/10.31399/asm.tb.spsp2.9781627082655
18. Yuzbekova, D., Mogucheva, A., Zhemchuzhnikova, D., Lebedkina, T., Lebyodkin, M., and Kaibyshev, R., Effect of Microstructure on Continuous Propagation of the Portevin–Le Chatelier Deformation Bands, *Int. J. Plasticity*, 2017, vol. 96, pp. 210–226. https://doi.org/10.1016/j.ijplas.2017.05.004
19. Jatczak, C.F., Retained Austenite and Its Measurement by X-Ray Diffraction, *SAE Trans*., 1980, pp. 1657–1676. https://doi.org/10.4271/800426
20. Dong, X.X., Shen, Y.F., Jia, N., and Zhu, Y.T., Improving Mechanical Properties and Retained-Austenite Stability of a Medium Carbon Q&P Steel by Adjusting Phase Ratio, *Mater. Sci. Eng. A*, 2022, vol. 833, p. 142580. https://doi.org/10.1016/j.msea.2021.142580
21. Li, Y., Chen, S., Wang, C., San Martín, D., and Xu, W., Modeling Tetained Austenite in Q&P Steels Accounting for the Bainitic Transformation and Correction of Its Mismatch on Optimal Conditions, *Acta Mater.*, 2020, vol. 188, pp. 528–538. https://doi.org/10.1016/j.actamat.2020.02.033
22. Seo, E.J., Cho, L., Kim, J.K., Mola, J., Zhao, L., and De Cooman, B.C., Constituent-Specific Properties in Quenching and Partitioning (Q&P) Processed Steel, *Mater. Sci. Eng. A*, 2019, vol. 740, pp. 439–444. https://doi.org/10.1016/j.msea.2018.10.082
23. Mishnev, R., Borisova, Y., Kniaziuk, T., Gaidar, S., and Kaibyshev, R., Quench and Tempered Embrittlement of Ultra-High-Strength Steels with Transition Carbides, *Metals*, 2023, vol. 13, no. 8, p. 1399. https://doi.org/10.3390/met13081399
24. Dhara, S., van Bohemen, S.M., and Santofimia, M.J., Isothermal Decomposition of Austenite in Presence of Martensite in Advanced High Strength Steels: A Review, *Mater. Today Commun.*, 2022, vol. 33, p. 104567. https://doi.org/10.1016/j.mtcomm.2022.104567
25. Okamoto, H. and Oka, M., Isothermal Martensite Transformation in a 1.80 wt % C Steel, *Metall. Trans. A*, 1985, vol. 16, pp. 2257–2262. https://doi.org/10.1007/BF02670425

26. Kumar, S. and Singh, S.B., Evolution of Microstructure during the "Quenching and Partitioning (Q&P)" Treatment, *Materialia*, 2021, vol. 18, p. 101135. https://doi.org/10.1016/j.mtla.2021.101135
27. Koistinen, D.P., A General Equation Prescribing Extend of Austenite–Martensite Transformation in Pure Fe-C Alloys and Plain Carbon Steels, *Acta Metallurg.*, 1959, vol. 7, pp. 50–60. https://cir.nii.ac.jp/crid/1571417125323684608
28. Andrews, K.W., Empirical Formulae for the Calculation of Some Transformation Temperatures, *J. Iron Steel Inst*., 1965, pp. 721–727. https://cir.nii.ac.jp/crid/1571980075716504064
29. Van Bohemen, S.M.C., Bainite and Martensite Start Temperature Calculated with Exponential Carbon Dependence, *Mater. Sci. Technol*., 2012, vol. 28, no. 4, pp. 487–495. https://doi.org/10.1179/1743284711Y.0000000097
30. Peng, F., Xu, Y., Gu, X., Wang, Y., Liu, X., and Li, J., The Relationships of Microstructure-Mechanical Properties in Quenching and Partitioning (Q&P) Steel Accompanied with Microalloyed Carbide Precipitation, *Mater. Sci. Eng. A*, 2018, vol. 723, pp. 247–258. https://doi.org/10.1016/j.msea.2018.03.061
31. Vercruysse, F., Celada-Casero, C., Linke, B.M., Verleysen, P., and Petrov, R.H., The Effect of Nb on the Strain Rate and Temperature Dependent Behaviour of Quenching & Partitioning Steels, *Mater. Sci. Eng. A*, 2021, vol. 800, p. 140293. https://doi.org/10.1016/j.msea.2020.140293
32. Mogucheva, A., Yuzbekova, D., Kaibyshev, R., Lebedkina, T., and Lebyodkin, M., Effect of Grain Refinement on Jerky Flow in an Al-Mg-Sc Alloy, *Metall. Mater. Trans. A*, 2016, vol. 47, pp. 2093–2106. https://doi.org/10.1007/s11661-016-3381-2
33. Timokhina, I.B., Hodgson, P.D., and Pereloma, E.V., Effect of Microstructure on the Stability of Retained Austenite in Transformation-Induced Plasticity Steels, *Metall. Mater. Trans. A*, 2004, vol. 35, pp. 2331–2341. https://doi.org/10.1007/s11661-006-0213-9
34. Kusakin, P., Belyakov, A., Haase, C., Kaibyshev, R., and Molodov, D.A., Microstructure Evolution and Strengthening Mechanisms of Fe-23Mn-0.3C-1.5Al TWIP Steel during Cold Rolling, *Mater. Sci. Eng. A*, 2014, vol. 617, pp. 52–60. https://doi.org/10.1016/j.msea.2014.08.051